Superconducting Switch for Fast On-Chip Routing of Quantum Microwave Fields

M. Pechal,* J.-C. Besse, M. Mondal, M. Oppliger, S. Gasparinetti, and A. Wallraff
Department of Physics, ETH Zurich, CH-8093 Zurich, Switzerland
(Received 3 June 2016; revised manuscript received 19 July 2016; published 11 August 2016)

A switch capable of routing microwave signals at cryogenic temperatures is a desirable component for state-of-the-art experiments in many fields of applied physics, including but not limited to quantum-information processing, communication, and basic research in engineered quantum systems. Conventional mechanical switches provide low insertion loss but disturb operation of dilution cryostats and the associated experiments by heat dissipation. Switches based on semiconductors or microelectromechanical systems have a lower thermal budget but are not readily integrated with current superconducting circuits. Here we design and test an on-chip switch built by combining tunable transmission-line resonators with microwave beam splitters. The device is superconducting and as such dissipates a negligible amount of heat. It is compatible with current superconducting circuit fabrication techniques, operates with a bandwidth exceeding 100 MHz, is capable of handling photon fluxes on the order of 10^5 μs^{-1}, equivalent to powers exceeding -90 dBm, and can be switched within approximately 6–8 ns. We successfully demonstrate operation of the device in the quantum regime by integrating it on a chip with a single-photon source and using it to route nonclassical itinerant microwave fields at the single-photon level.

DOI: 10.1103/PhysRevApplied.6.024009

I. INTRODUCTION

Many fields of research ranging from material physics to quantum-information processing make use of microwave measurements at temperatures as low as a few tens of millikelvin. To build microwave systems capable of operation at these low temperatures often requires the use of components specifically designed for such conditions. For active devices such as amplifiers, the usual semiconductor-based designs dissipate too much power to be compatible with millikelvin temperatures [1], necessitating alternative approaches such as superconducting devices based on parametric amplification [2,3].

A rf switch is another example of a device commonly used in room-temperature microwave systems, whose integration in cryogenic setups is problematic. Latching mechanical switches have been successfully used for setups inside dilution refrigerators [4], but the heat load due to the solenoids used for moving the mechanical parts causes significant increase in temperature after each switching event and a rather long time of approximately 15 min is needed for the cryostat to reach its base temperature again. Positive-intrinsic-negative (p-i-n) diode switches which need to be continuously current biased during operation are even less suitable for low-temperature applications. The quickly developing family of MEMS microwave switches [5,6] can provide very reliable switching with a minimal power dissipation and seem to be good candidates for cryogenic microwave setups [7,8]. Similarly promising devices were recently demonstrated based on field-effect transistors [9–12]. However, these types of switches cannot be easily combined with on-chip superconducting circuits without a significant modification of the fabrication process.

On-chip switching devices will be a useful tool for construction of more complex integrated quantum systems and have a potential to enable a range of experiments. For example, in combination with measurement-based entanglement-generation techniques, such as demonstrated in Ref. [13], they can be used to create distributed multiqubit entangled states. In experiments of the Hong-Ou-Mandel type [14], microwave-field states can be routed in a network of switches and beam splitters to generate a range of different nonclassical states using a single device. The ability to route signals on chip can also provide a convenient way to calibrate a linear detection setup by fabricating a suitable source of a reference signal on the same chip as the device under test.

Here we describe and experimentally test a microwave switch design which is integrated on a superconducting chip using fabrication procedures widely employed in the field of superconducting quantum circuits. Devices of a similar type were recently implemented [15–18] but are currently restricted to the single-pole, single-throw mode of operation. That is, they can either route a signal towards an output port or reflect it back to the input. In contrast, our switch is of the single-pole, double-throw type; it switches a single input to one of two outputs or vice versa. The device is based on interference effects in a microwave circuit and has no moving parts. The expected internal loss rate in a superconducting circuit of this type [19] is at least 3 orders of magnitude lower than the 3-dB bandwidth,

*mpechal@phys.ethz.ch

which is on the order of 100 MHz in the device studied here. This bandwidth is smaller than that of mechanical or *p-i-n* diode switches but sufficient for many applications encountered in superconducting circuit experiments. The device is controlled by externally applied magnetic flux which, if generated by an on-chip flux line, can be tuned on time scales of a few nanoseconds [20], making the switching very fast as compared to typical coherence times of state-of-the-art superconducting circuits. This fast tunability will make it useful in applications where routing of signals needs to be controlled by real-time feedback.

II. PRINCIPLE OF OPERATION

The switch consists of two $\pi/2$ hybrid couplers [14], [[21], p. 343] connected in a Mach-Zehnder-like configuration with two independently tunable coplanar waveguide resonators [19,22] in the two arms, as shown in Fig. 1(a). The resonance frequencies of the resonators are tuned by changing the inductance of two arrays of $N = 5$ superconducting quantum-interference-device (SQUID) loops placed in their centers [23]. The inductance of these arrays depends on a magnetic flux applied using two superconducting coils. The hybrid coupler is a structure consisting of four transmission-line segments of equal length with pairwise equal characteristic impedances arranged in a square [see Fig. 1(c)]. Its effect on an incident microwave signal is analogous to that of an optical beam splitter, but the phases of the two resulting signals are phase shifted with respect to each other by $\pi/2$. The hybrid lends itself to a straightforward implementation in the planar architecture of superconducting circuits where it has been used for quantum optics experiments with single microwave photons [14].

For the following discussion, we number the ports of the device according to Fig. 1(a). The signal entering port 1 of the top hybrid is split equally into its two output ports and arrives at the resonators. When both of them are far detuned from the signal frequency, they act as nearly perfect reflectors [see Fig. 1(b)]. Because of the phase relation between the outputs of the hybrid, the two reflected parts of the signal recombine in port 2. This situation corresponding to what we will call the *off-resonant state* of the switch is schematically illustrated by solid arrows in Fig. 1(a). Conversely, in the *resonant state*, both resonators are fully transmittive [see Fig. 1(b)], and the signal arriving at the bottom hybrid will recombine in port 3, as shown by the dashed arrows in Fig. 1(a).

An array of N SQUID loops can be approximated as an inductor of inductance $L = N\hbar^2/(4e^2E_J)$, where E_J is the Josephson energy of each SQUID related to the Josephson energies E_{J1}, E_{J2} of the junctions comprising the SQUID and the magnetic flux Φ threading the loop by $E_J = \sqrt{E_{J1}^2 + E_{J2}^2 + 2E_{J1}E_{J2}\cos(2e\Phi/\hbar)}$. The approximation by an inductor is valid only in the limit where the currents flowing across the junctions are small in comparison with their critical currents, that is, for

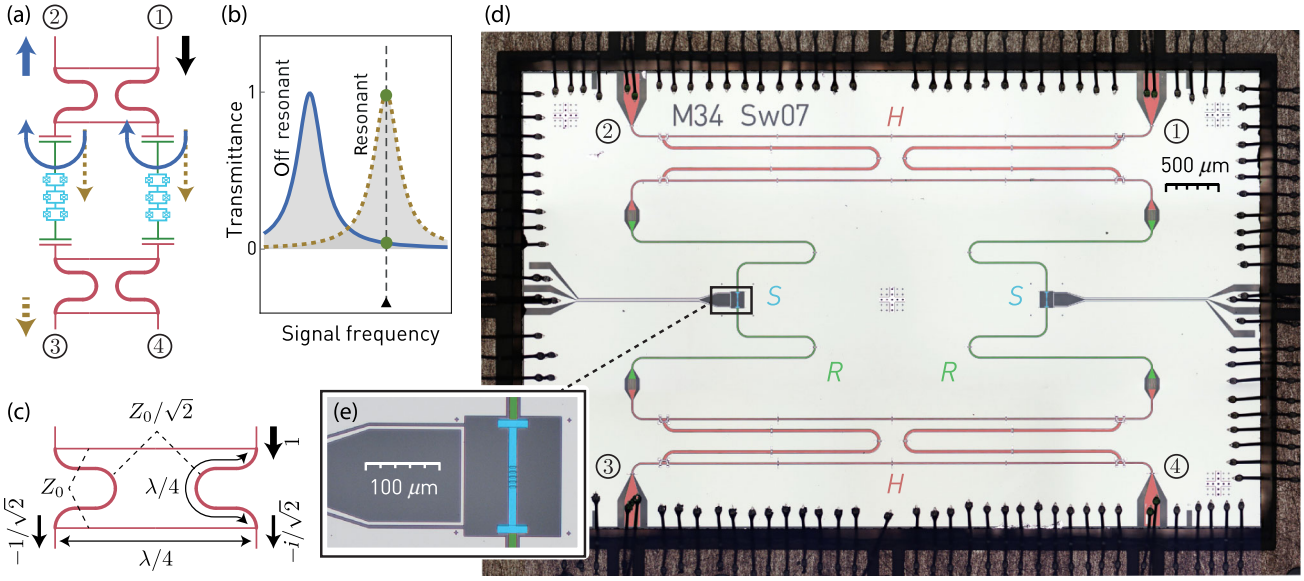

FIG. 1. (a) Schematic diagram of the switch illustrating the two switch states. The path taken by the signal is shown for the resonators off resonant (solid arrows) and resonant (dashed arrows) with the signal. Input and output ports are labeled by 1,2,3,4. (b) The theoretically expected transmittance of the resonators for the off-resonant and resonant switch states shown in (a). The signal frequency is indicated by the thin dashed line, the corresponding values of the transmittance by the green points. (c) Schematic diagram of the $\pi/2$ hybrid and the relevant S parameters at the operating frequency. (d) False-color micrograph of the sample mounted on its printed circuit board with the $\pi/2$ hybrids (H) indicated in red, the transmission line resonators (R) in green, and the SQUID arrays (S) in blue. (e) Enlarged view of the SQUID array with the flux line loop visible on the left.

sufficiently low signal powers. At higher powers, nonlinear effects cause compression of the transmitted signal [24,25].

Using an array rather than a single SQUID loop improves the linearity of the device [22,26] for the following reason. To achieve a given inductance L with a series combination of N SQUID loops, the required inductance of each single loop scales as $1/N$, and the corresponding Josephson energy E_J is, therefore, proportional to N. The phase difference across the array is divided into N equal parts $\delta \propto 1/N$, and the first higher-order term in the energy of each loop, therefore, scales as $E_J\delta^4 \propto N \times (1/N)^4$. The leading term in the Hamiltonian describing the nonlinearity of the device then scales as $NE_J\delta^4 \propto 1/N^2$. Thus, the linearity of the device is improved by increasing N. Our choice of $N = 5$ [see Fig. 1(e)] is a compromise between suppression of nonlinear effects, which favors high N, and uniformity of the magnetic flux through the individual SQUID loops of the array, which is harder to achieve when the array is made longer.

III. MEASUREMENT SETUP AND DEVICE PARAMETERS

The switch is fabricated on a (7×4)-mm sapphire chip with the coplanar waveguide structures patterned by photolithography and etching of a niobium film [see Fig. 1(d)]. Air bridges made in an additional optical lithography step by deposition of aluminum and titanium are distributed along the transmission lines to suppress potential parasitic modes on the chip. The process to fabricate these is extensively used in our lab [14,27] and is similar to the one described in Ref. [28]. The SQUID arrays [see Fig. 1(e)] are fabricated by electron-beam lithography and shadow evaporation of aluminum. A test chip with resonators in which the SQUIDs are replaced by an equally sized niobium strip directly connecting the two resonator halves is measured in a dipstick at 4.2 K to determine the effective length of the resonator. The obtained resonance frequency of the fundamental mode is $\omega_{r0}/2\pi = 8.30$ GHz and its 3-dB bandwidth $\kappa_0/2\pi = 305$ MHz. In another test measurement at 4.2 K, the operating frequency of the hybrid couplers is found to be $\omega_h/2\pi = 7.2$ GHz. The SQUID arrays consist of $N = 5$ loops with a designed asymmetry ratio $E_{J1}:E_{J2} = 2:3$ chosen to yield a tuning ratio between the minimum and maximum E_J of 1:5. The areas of the junctions in the SQUID array are approximately 2–3 μm^2. The resulting frequency tuning range of the resonator of 5.5–7.5 GHz is sufficient to fine-tune the device to its optimal operating point but not much larger than necessary. This property helps to keep the sensitivity of the resonator frequencies to external magnetic flux noise low. The Josephson energies of the two junctions extracted from a measurement of the flux dependence of the resonator frequency (see the Supplemental Material [23]) are $E_{J1}/h = 1.06$ THz and $E_{J2}/h = 1.54$ THz, respectively, corresponding to critical currents of $I_{c1} = 2.13$ μA and $I_{c2} = 3.10$ μA. The equivalent critical current density is close to 100 A/cm^2.

The experimental setup used in the initial characterization measurements of the switch is shown in Fig. 2. The device is mounted at the base plate of a dilution refrigerator and cooled down to a temperature of 30 mK. Its ports 1, 2, and 3 are connected to three input lines and one output line through a circulator as indicated in the figure. The remaining port 4 is terminated with a 50-Ω load. We measure the amplitude of the output signal using heterodyne detection with an intermediate frequency of 25 MHz. To obtain the normalized S parameters S_{11}, S_{12}, and S_{13}, the measured signal amplitude is calibrated using reference measurements at full transmission and reflection. These are taken at the base temperature of the cryostat with the sample removed and with the end of microwave line 1 left

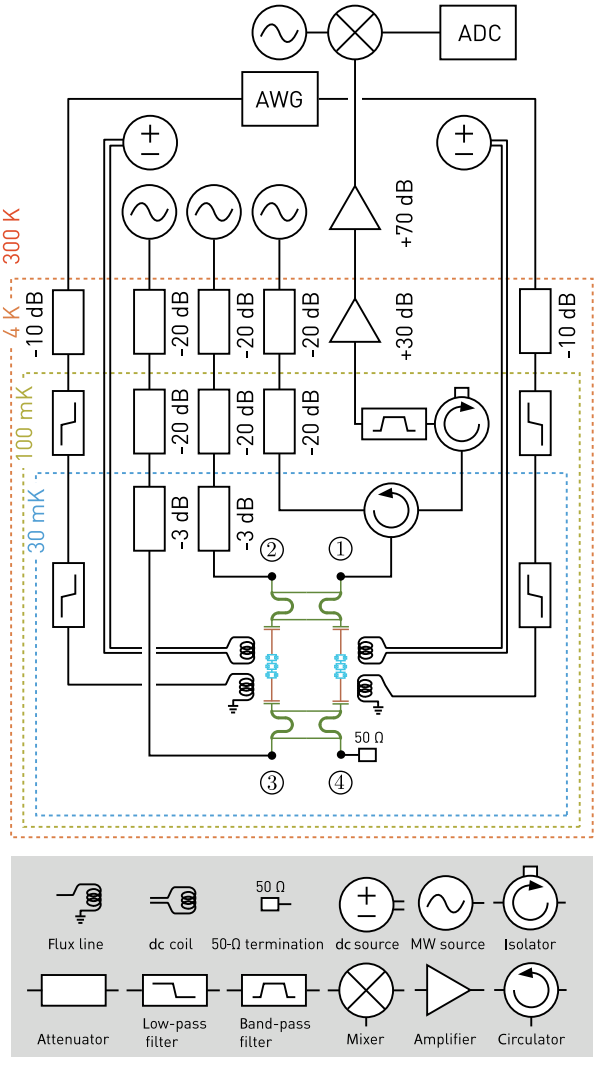

FIG. 2. Schematic diagram of the experimental setup with the relevant temperature stages of the dilution refrigerator indicated by the dashed boxes.

open or with lines 2 or 3 connected via a short coaxial through to line 1.

Magnetic flux bias of the SQUID arrays to tune the resonator frequencies is realized using two dc superconducting coils mounted on the sample holder underneath the two SQUID arrays. To achieve fast control of the flux, we use two on-chip flux lines [see Figs. 1(d), 1(e), and 2] connected to an arbitrary waveform generator (AWG) with a bandwidth of 500 MHz.

IV. RESULTS

A. Characterization in the classical regime

To characterize the device, we first measure the transmission coefficient S_{12} as a function of frequency. We expect this coefficient to be close to unity when both resonators are far detuned from the signal and to decrease when either of the resonators is driven resonantly. By doing this measurement for different bias voltages applied to one of the two coils, we observe how the resonance frequencies change with magnetic field. The two lines visible in the measured dependence plotted in Fig. 3(a) correspond to the two resonators which couple to the coil with different strengths. The strongly coupled resonator shows approximately periodic behavior of its frequency, as expected from the dependence of the SQUID loop Josephson energy on magnetic flux. The imperfect periodicity is consistent with a small inhomogeneity of the magnetic field threading the different loops in the array. A fit based on a model taking this inhomogeneity into account [23] shown in Fig. 3(a) by the dashed line matches the data with good accuracy.

We set the signal frequency to 7.2 GHz—the working frequency of the hybrid couplers—and find the operating points of the switch by sweeping the bias voltages of both coils. We identify the two pairs of voltages for which the branching ratio S_{12}/S_{13} is maximal and minimal. These operating points correspond to the off-resonant and the resonant state of the switch, respectively.

The ability of the switch to block signal transmission into the unwanted port can be characterized by the on:off ratios $|S_{12}^{(\mathrm{on})}/S_{12}^{(\mathrm{off})}|^2$ and $|S_{13}^{(\mathrm{off})}/S_{13}^{(\mathrm{on})}|^2$ between the transmitted powers in the resonant (superscript "on") and off-resonant state (superscript "off"). We evaluate these at the operating frequency of 7.2 GHz and obtain the values 28 and 32 dB, respectively. We expect that this suppression of approximately 3 orders of magnitude in power can be improved by increasing the tuning range of the resonators and optimizing the $\pi/2$ hybrid parameters.

We estimate the bandwidth of the switch by measuring the transmission coefficients S_{12} and S_{13} as a function of frequency at the two operating points of the device, obtaining the data shown in Figs. 3(b) and 3(c). We see that in the off-resonant state (blue), the coefficients are relatively insensitive to frequency changes. This is to be expected because the signal is detuned from the resonance

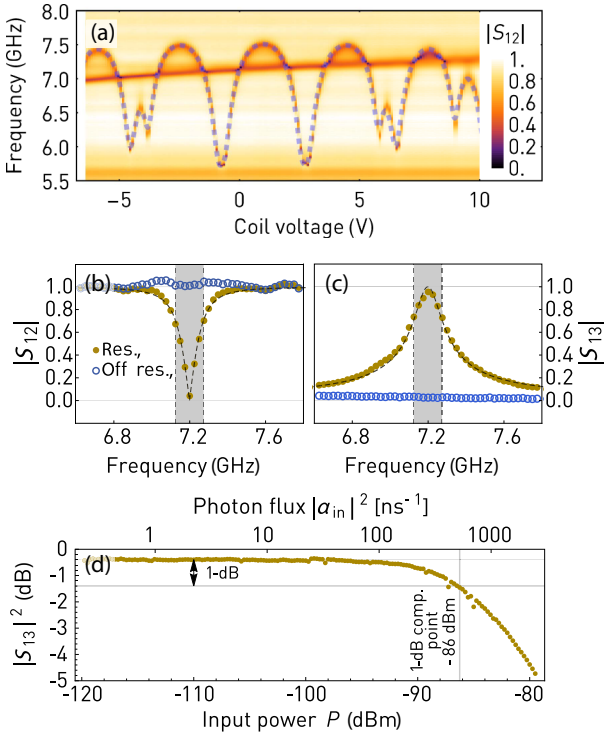

FIG. 3. (a) Transmission coefficient S_{12} as a function of frequency and voltage applied to one of the flux bias coils. The dashed line represents a fit to a theoretical model [23]. Measured frequency dependence of (b) the S_{12} and (c) the S_{13} transmission coefficients in the off-resonant state (empty blue circles) and the resonant state (filled yellow circles) of the switch. The values slightly larger than 1 result from imperfections of the calibration procedure. The gray band indicates the bandwidth of the device. (d) The $|S_{13}|^2$ transmittance on resonance (at 7.2 GHz) in the resonant state of the switch as a function of the power (or, equivalently, the photon flux $|\alpha_{\mathrm{in}}|^2$) estimated at the input of the device.

frequencies of the two resonators by more than 1 GHz, that is, by nearly 10 times their linewidth. On the other hand, in the resonant state, the bandwidth of the device is determined by the linewidth of the tunable resonators. As seen in Figs. 3(b) and 3(c), the data closely match the fitted Lorentzian frequency response $|S_{13}|^2 = 1 - |S_{12}|^2 = 1/[1 + 4(f - f_0)^2/\Delta f^2]$ shown by the dashed line. The center frequency $f_0 = 7.20$ GHz and the bandwidth $\Delta f = \kappa/2\pi = 149$ MHz are extracted from the fit.

To characterize the impedance matching of the device, we measure the signal reflected from port 1 for both states of the switch. To account for reflections due to setup imperfections rather than the device itself, we compare the results with a reference measurement obtained when the device is removed and the connector of port 1 is terminated with a cryogenic 50-Ω load, resulting in full absorption of the signal at the port. The power reflectance observed in this reference measurement is below −10 dB within the 150-MHz wide band of the switch, and we observe no

systematic increase in this value when the device is connected, confirming that the reflections from the switch are small in comparison with the setup reflections.

We determine the linear operating range of the device by tuning it into the resonant state, probing it resonantly, and observing the transmittance between ports 3 and 1 as a function of the applied power. The measured data presented in Fig. 3(d) show constant $|S_{13}|^2$ for powers lower than approximately -100 dBm and a progressively higher compression as the power is increased. This nonlinear effect can be quantified in terms of the 1-dB compression point–the power at the input of the device at which the transmittance is reduced by 1 dB with respect to the low-power limit. To estimate the power level at the input port of the switch from the power generated by the microwave source, we measure the transmittivity of the input cables with a vector network analyzer. However, since this reference measurement is taken at room temperature and the actual transmittance is likely to be higher due to reduced losses of the microwave components at low temperatures, the power calculated in this way most likely underestimates the actual power by a few decibels. As shown in Fig. 3(d), the 1-dB compression point extracted from the data is approximately -86 dBm, that is 2.3 pW or approximately 5×10^5 photons per microsecond at 7.2 GHz. The nonlinearity of the device can also be estimated theoretically from the properties of the Josephson junctions forming the SQUID array, as expressed by Eq. (6) derived in the Supplemental Material [23]. This equation together with the experimentally estimated junction parameters yield the Kerr nonlinearity $K/2\pi = 28$ kHz and the compression point $P_{\mathrm{CP}} = -81$ dBm for this device. This agrees reasonably well with the measured value, and we suspect the observed difference of 5 dB to be caused by the reduced losses in the microwave lines at low temperatures.

To study the switching speed at shorter time scales than those achievable with the magnetic field coils, we use on-chip flux lines [see Figs. 1(d), 1(e), and 2] connected to the outputs of an arbitrary waveform generator capable of synthesizing waveforms with a bandwidth of 500 MHz. We first set the bias voltages of the coils to bring the switch to the resonant state in absence of any current through the flux lines. We then apply square pulses of varying amplitude to the flux lines to determine the voltages needed to switch the device to the off-resonant state. These voltages are again found as those corresponding to the maximum of the branching ratio S_{12}/S_{13}.

We set up a measurement where a continuous signal at a frequency of 7.2 GHz is applied to either one of the ports 2 and 3 and the output measured at port 1. Then we modulate the flux line voltages with a square pulse and record the down-converted waveforms (see Fig. 4). For this measurement, we use a higher-bandwidth detection system with an intermediate frequency of 250 MHz and analog bandwidth of 500 MHz [23].

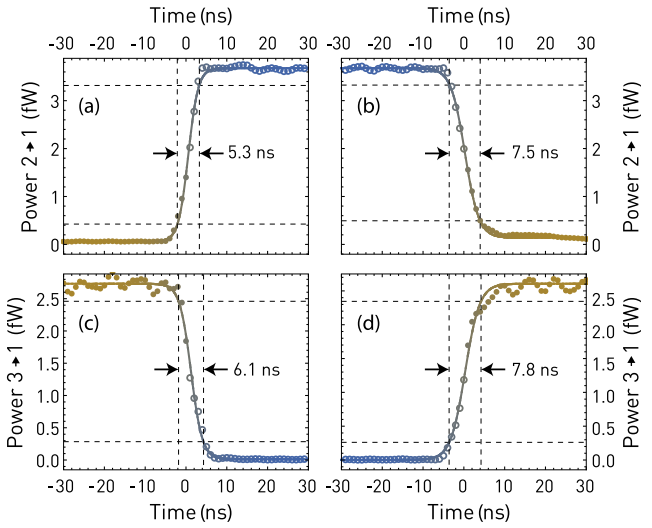

FIG. 4. Recorded waveforms of the (a) rising and (b) falling edges of the signal transmitted between ports 2 and 1 and between ports 3 and 1 (c), (d). The colors of the points represent the two switch states as shown in Figs. 1 and 3. Solid lines are fits to a tanh step used to estimate the rise or fall times. Dashed lines represent the 10% and 90% signal levels used to extract the indicated switching times.

As shown in Fig. 4, we fit a tanh step to the measured waveforms to extract the 10%–90% rise and fall times of approximately 5 and 7 ns for the signal applied at port 2 and 8 and 6 ns for the signal applied at port 3.

B. Switching of quantum signals

In order to simultaneously demonstrate the operation of the switch at the quantum level and its integrability with other quantum devices, we fabricate a sample combining it with a single-photon source on the same chip, as seen in Fig. 5. The source is of the type demonstrated in Ref. [29]. It is implemented as a transmon-type superconducting qubit directly capacitively coupled to an input line of the switch and, with a weaker coupling, to a control line used to excite the qubit. The resonance frequency of the qubit is tuned by a magnetic flux applied using a superconducting coil such that the frequency of the emitted photon matches the optimal operating frequency of the switch at 7.2 GHz. The charging energy and Josephson energy of the qubit at this frequency are $E_C/h = 220$ MHz and $E_J/h = 32$ GHz.

The qubit is first excited by applying a short (approximately 10 ns) microwave pulse rotating its Bloch vector by an angle θ proportional to the pulse amplitude. This prepares the qubit in a superposition state of the ground state and the first excited state. When the qubit subsequently relaxes by photon emission into the input line of the switch, its state is mapped onto the corresponding superposition of the vacuum state $|0\rangle$, and the single-photon Fock state $|1\rangle$ of the propagating field. The photon state generated in this way has an exponential envelope

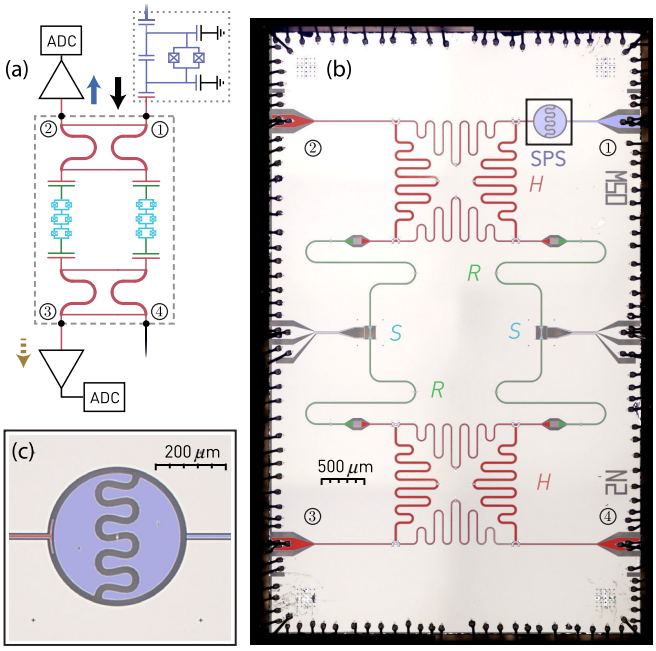

FIG. 5. (a) Diagram of the sample combining the switch (dashed box) with a transmon-based single-photon source (dotted box). The detection chain represented by the triangular amplifier symbol uses a Josephson parametric amplifier for near-quantum-limited measurements. (b) False-color optical image of the sample wire bonded on its printed circuit board, with the resonators (R) in green, $\pi/2$ hybrids (H) in red, SQUID arrays (S) in cyan, and the single-photon source (SPS) in blue. The design of the $\pi/2$ hybrid is more compact than in the first-generation switch to enable better scaling in future devices. (c) Enlarged view of the single-photon source with the two half-circular capacitor pads joined by the SQUID loop in the center. The weakly coupled drive line is shown in blue on the right, and the strongly coupled output line in red on the left.

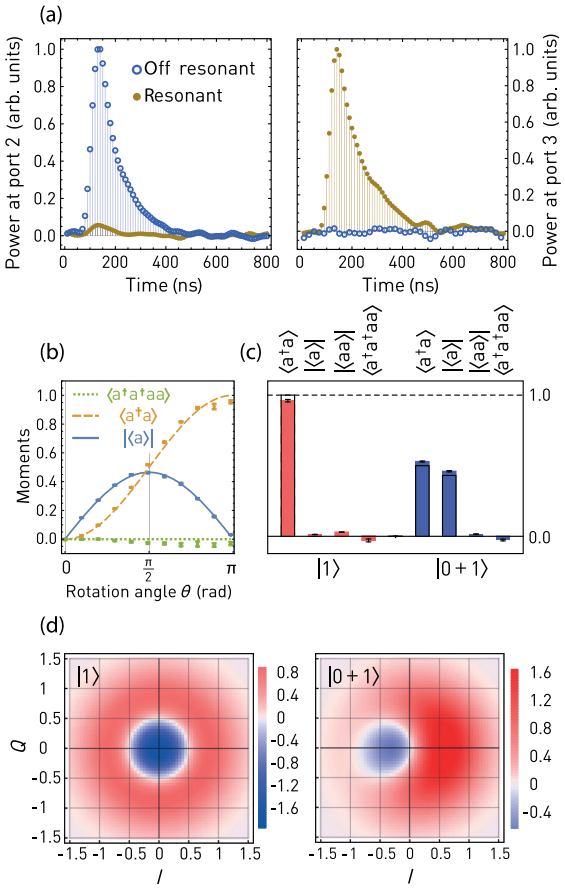

FIG. 6. (a) The single-photon power waveforms measured at the output ports 2 (left) and 3 (right) in the resonant (filled yellow points) and off-resonant (empty blue points) state of the switch. (b) Calibration measurements of the moments $|\langle a\rangle|$, $a^\dagger a$, and $a^\dagger a^\dagger aa$ as a function of the rotation angle in the qubit initialization step. (c) Measured moments of a single-photon state $|1\rangle$ (red) and a superposition state $(|0\rangle + |1\rangle)/\sqrt{2}$ (blue) transmitted through the switch. (d) Wigner functions corresponding to the moments from (c) obtained from them using a maximum likelihood method.

with a time constant of approximately 90 ns. The couplings to the qubit drive and switch input lines are designed to be sufficiently asymmetric such that the probability of the photon being emitted into the qubit drive line is only approximately 2%. The relaxation time constant of the qubit estimated from a finite-element simulation of the design is 74 ns. This is slightly shorter than the measured value, possibly due to fabrication imprecisions affecting the coupling capacitance which is rather sensitive to the size of the gap between the qubit and the switch input line. When designing the single-photon source, we also engineer the direct coupling between the input and the output to be sufficiently weak to make the mean number of photons transmitted during the excitation pulse negligible. For this particular design, we estimate this number to be approximately 0.03.

After routing the single-photon state through the switch, we measure the signal power at its two outputs in both of its states. This is done by averaging the square of the measured voltage and subtracting the noise power obtained in an identical measurement with the signal source turned off [30]. The resulting waveforms are shown in Fig. 6(a) and demonstrate that the photon can be successfully routed to either one of the outputs.

By calculating the moments of the measured single-shot voltages and systematically subtracting the reference values measured in the absence of the signal, as outlined for example in Ref. [31], we extract the moments of the photon mode a. Figure 6(b) shows the moments $|\langle a\rangle|$, $\langle a^\dagger a\rangle$, and $\langle a^\dagger a^\dagger aa\rangle$ of the emitted field as a function of the rotation angle θ used in the qubit initialization step. We use these data to find the normalization coefficient for the moment measurements [23]. The measured moments are in close agreement with theory where the photon number $\langle a^\dagger a\rangle$ is expected to vary as $\sin^2(\theta/2)$ and the coherence $|\langle a\rangle|$ as $|\sin\theta|$.

In particular, we analyze the Fock state $|1\rangle$ and the superposition state $(|0\rangle + |1\rangle)/\sqrt{2}$ (which we denote for the sake of brevity by $|0+1\rangle$) whose relevant moments are shown in Fig. 6(c). The first- and second-order moments agree well with the expected values $\langle a^\dagger a\rangle = 1$, $|\langle a\rangle| = 0$ for $|1\rangle$, and $\langle a^\dagger a\rangle = 1/2$, $|\langle a\rangle| = 1/2$ for $|0+1\rangle$. The slightly reduced value of $|\langle a\rangle| \approx 0.46$ for $|0+1\rangle$ can be explained as a result of dephasing of the photon-source qubit which leads to a prediction of $|\langle a\rangle| \approx 0.43$. As expected for a single-photon field, as opposed to a coherent or thermal state, the higher-order moments such as $\langle aa\rangle$ or $\langle a^\dagger a^\dagger aa\rangle$ are close to zero.

Of particular interest is the normalized zero-time-delay intensity correlation function $g^{(2)} = \langle a^\dagger a^\dagger aa\rangle/\langle a^\dagger a\rangle^2$. Its value of -0.03 ± 0.01 for $|1\rangle$ and -0.09 ± 0.02 for $|0+1\rangle$ is very close to zero, showing nearly ideal antibunching of the switched microwave field. The fact that the value extracted from the experiments is slightly negative is most likely an artifact of the data analysis procedure which we ascribe to a nonvanishing thermal field in the off measurement used as a reference. The nonclassical nature of the switched signal is corroborated by the negative values of the Wigner function [32] shown in Fig. 6(d), which is extracted from the measured moments by means of a maximum likelihood method [31,33].

V. CONCLUSIONS

We describe the design, realization, and characterization of an on-chip superconducting microwave switch and demonstrate that this device can be integrated in experiments at cryogenic temperatures, such as, for example, in the field of quantum-information processing with superconducting qubits. The switching is based on interference effects in a circuit with two hybrid couplers and two resonators tunable by an externally applied magnetic field. The device studied here operates optimally at 7.2 GHz, has a bandwidth of 150 MHz, an isolation of 30 dB, and is well impedance matched to 50 Ω. The resonators are designed to have low anharmonicity, allowing the switch to route approximately 5×10^5 microwave photons per microsecond at its 1-dB compression point. An on-chip flux line allows us to perform switching on a nanosecond time scale. We integrate the device on a chip with a single-photon source and demonstrate its operation in the quantum regime by switching propagating Fock states and their coherent superpositions.

We expect this device to have a variety of uses in applications requiring fast multiplexing or demultiplexing of microwave signals directly at the mixing chamber stage of a dilution refrigerator. For example, it may be used for controlling and reading out multiple quantum systems with a small number of rf input and output lines, as an alternative to frequency multiplexing [34]. It should also present a convenient calibration tool for normalizing S-parameter measurements in the cryostat [4] or characterizing linear detection chains in absolute photon-number terms by switching between the device under test and a suitable reference source [29,35]. It can also be useful for building configurable networks for quantum-optics experiments with microwaves [36], remote entanglement distribution, or quantum communication [37,38].

ACKNOWLEDGMENTS

We would like to thank Patrice Bertet, Sebastian Probst, Benjamin Chapman, and Eric Rosenthal for useful comments on the manuscript. This work is supported by the European Research Council through the "Superconducting Quantum Networks" project, by National Centre of Competence in Research "Quantum Science and Technology," a research instrument of the Swiss National Science Foundation, and by ETH Zurich.

[1] M. W. Pospieszalski, S. Weinreb, R. D. Norrod, and R. Harris, FET's and HEMT's at cryogenic temperatures—their properties and use in low-noise amplifiers, IEEE Trans. Microwave Theory Tech. **36**, 552 (1988).

[2] Bernard Yurke and Eyal Buks, Performance of cavity-parametric amplifiers, employing Kerr nonlinearites, in the presence of two-photon loss, J. Lightwave Technol. **24**, 5054 (2006).

[3] M. A. Castellanos-Beltran and K. W. Lehnert, Widely tunable parametric amplifier based on a superconducting quantum interference device array resonator, Appl. Phys. Lett. **91**, 083509 (2007).

[4] Leonardo Ranzani, Lafe Spietz, Zoya Popovic, and Jose Aumentado, Two-port microwave calibration at millikelvin temperatures, Rev. Sci. Instrum. **84**, 034704 (2013).

[5] G. M. Rebeiz and J. B. Muldavin, RF MEMS switches and switch circuits, IEEE Microw. Mag. **2**, 59 (2001).

[6] B. Schoenlinner, A. Stehle, C. Siegel, W. Gautier, B. Schulte, S. Figur, U. Prechtel, and V. Ziegler, The low-complexity RF MEMS switch at EADS: An overview, Int. J. Microwave Wireless Technol. **3**, 499 (2011).

[7] S. Gong, H. Shen, and N. S. Barker, Study of broadband cryogenic dc-contact RF MEMS switches, IEEE Trans. Microwave Theory Tech. **57**, 3442 (2009).

[8] S. S. Attar, S. Setoodeh, R. R. Mansour, and D. Gupta, Low-temperature superconducting dc-contact RF MEMS switch for cryogenic reconfigurable RF front-ends, IEEE Trans. Microwave Theory Tech. **62**, 1437 (2014).

[9] H. Al-Taie, L. W. Smith, B. Xu, P. See, J. P. Griffiths, H. E. Beere, G. A. C. Jones, D. A. Ritchie, M. J. Kelly, and C. G. Smith, Cryogenic on-chip multiplexer for the study of quantum transport in 256 split-gate devices, Appl. Phys. Lett. **102**, 243102 (2013).

[10] D. R. Ward, D. E. Savage, M. G. Lagally, S. N. Coppersmith, and M. A. Eriksson, Integration of on-chip field-effect transistor switches with dopantless Si/SiGe quantum dots for high-throughput testing, Appl. Phys. Lett. **102**, 213107 (2013).

[11] R. K. Puddy, L. W. Smith, H. Al-Taie, C. H. Chong, I. Farrer, J. P. Griffiths, D. A. Ritchie, M. J. Kelly, M. Pepper, and C. G. Smith, Multiplexed charge-locking device for large arrays of quantum devices, Appl. Phys. Lett. **107**, 143501 (2015).

[12] J. M. Hornibrook, J. I. Colless, I. D. Conway Lamb, S. J. Pauka, H. Lu, A. C. Gossard, J. D. Watson, G. C. Gardner, S. Fallahi, M. J. Manfra, and D. J. Reilly, Cryogenic Control Architecture for Large-Scale Quantum Computing, Phys. Rev. Applied **3**, 024010 (2015).

[13] A. Narla, S. Shankar, M. Hatridge, Z. Leghtas, K. M. Sliwa, E. Zalys-Geller, S. O. Mundhada, W. Pfaff, L. Frunzio, R. J. Schoelkopf, and M. H. Devoret, Robust concurrent remote entanglement between two superconducting qubits, arXiv:1603.03742.

[14] C. Lang, C. Eichler, L. Steffen, J. M. Fink, M. J. Woolley, A. Blais, and A. Wallraff, Correlations, indistinguishability and entanglement in Hong-Ou-Mandel experiments at microwave frequencies, Nat. Phys. **9**, 345 (2013).

[15] S. Schuermans, M. Simoen, M. Sandberg, P. Krantz, C. M. Wilson, and P. Delsing, An on-chip Mach-Zehnder interferometer in the microwave regime, IEEE Trans. Appl. Supercond. **21**, 448 (2011).

[16] Yi Yin, Yu Chen, Daniel Sank, P. J. J. O'Malley, T. C. White, R. Barends, J. Kelly, Erik Lucero, Matteo Mariantoni, A. Megrant, C. Neill, A. Vainsencher, J. Wenner, Alexander N. Korotkov, A. N. Cleland, and John M. Martinis, Catch and Release of Microwave Photon States, Phys. Rev. Lett. **110**, 107001 (2013).

[17] O. Naaman, M. O. Abutaleb, C. Kirby, and M. Rennie, On-chip Josephson junction microwave switch, Appl. Phys. Lett. **108**, 112601 (2016).

[18] Benjamin J. Chapman, Bradley A. Moores, Eric I. Rosenthal, Joseph Kerckhoff, and K. W. Lehnert, General purpose multiplexing device for cryogenic microwave systems, Appl. Phys. Lett. **108**, 222602 (2016).

[19] M. Göppl, A. Fragner, M. Baur, R. Bianchetti, S. Filipp, J. M. Fink, P. J. Leek, G. Puebla, L. Steffen, and A. Wallraff, Coplanar waveguide resonators for circuit quantum electrodynamics, J. Appl. Phys. **104**, 113904 (2008).

[20] M. Sandberg, C. M. Wilson, F. Persson, T. Bauch, G. Johansson, V. Shumeiko, T. Duty, and P. Delsing, Tuning the field in a microwave resonator faster than the photon lifetime, Appl. Phys. Lett. **92**, 203501 (2008).

[21] D. M. Pozar, *Microwave Engineering*, 4th ed. (John Wiley & Sons, Inc., New York, 2011).

[22] A. Palacios-Laloy, F. Nguyen, F. Mallet, P. Bertet, D. Vion, and D. Esteve, Tunable resonators for quantum circuits, J. Low Temp. Phys. **151**, 1034 (2008).

[23] See Supplemental Material at http://link.aps.org/supplemental/10.1103/PhysRevApplied.6.024009 for further details on the setup and measurement methods.

[24] P. Bertet, F. R. Ong, M. Boissonneault, A. Bolduc, F. Mallet, A. C. Doherty, A. Blais, D. Vion, and D. Esteve, Circuit quantum electrodynamics with a nonlinear resonator, arXiv:1111.0501v1.

[25] Fluctuating Nonlinear Oscillators, edited by M. Dykman (Oxford University Press, New York, 2012).

[26] Christopher Eichler and Andreas Wallraff, Controlling the dynamic range of a Josephson parametric amplifier, EPJ Quantum Technol. **1**, 2 (2014).

[27] Lars Steffen, Ph.D. thesis, ETH Zurich, 2013.

[28] Zijun Chen, A. Megrant, J. Kelly, R. Barends, J. Bochmann, Yu Chen, B. Chiaro, A. Dunsworth, E. Jeffrey, J. Y. Mutus, P. J. J. O'Malley, C. Neill, P. Roushan, D. Sank, A. Vainsencher, J. Wenner, T. C. White, A. N. Cleland, and John M. Martinis, Fabrication and characterization of aluminum airbridges for superconducting microwave circuits, Appl. Phys. Lett. **104**, 052602 (2014).

[29] Z. H. Peng, J. S. Tsai, and O. V. Astafiev, Tuneable on-demand single-photon source, arXiv:1505.05614.

[30] D. Bozyigit, C. Lang, L. Steffen, J. M. Fink, C. Eichler, M. Baur, R. Bianchetti, P. J. Leek, S. Filipp, M. P. da Silva, A. Blais, and A. Wallraff, Antibunching of microwave-frequency photons observed in correlation measurements using linear detectors, Nat. Phys. **7**, 154 (2011).

[31] C. Eichler, D. Bozyigit, and A. Wallraff, Characterizing quantum microwave radiation and its entanglement with superconducting qubits using linear detectors, Phys. Rev. A **86**, 032106 (2012).

[32] K. E. Cahill and R. J. Glauber, Density operators and quasiprobability distributions, Phys. Rev. **177**, 1882 (1969).

[33] D. F. V. James, P. G. Kwiat, W. J. Munro, and A. G. White, Measurement of qubits, Phys. Rev. A **64**, 052312 (2001).

[34] Y. Chen, D. Sank, P. O'Malley, T. White, R. Barends, B. Chiaro, J. Kelly, E. Lucero, M. Mariantoni, A. Megrant, C. Neill, A. Vainsencher, J. Wenner, Y. Yin, A. N. Cleland, and J. M. Martinis, Multiplexed dispersive readout of superconducting phase qubits, Appl. Phys. Lett. **101**, 182601 (2012).

[35] A. A. Houck, D. I. Schuster, J. M. Gambetta, J. A. Schreier, B. R. Johnson, J. M. Chow, L. Frunzio, J. Majer, M. H. Devoret, S. M. Girvin, and R. J. Schoelkopf, Generating single microwave photons in a circuit, Nature (London) **449**, 328 (2007).

[36] Y.-F. Chen, D. Hover, S. Sendelbach, L. Maurer, S. T. Merkel, E. J. Pritchett, F. K. Wilhelm, and R. McDermott, Microwave Photon Counter Based on Josephson Junctions, Phys. Rev. Lett. **107**, 217401 (2011).

[37] W. J. Munro, K. A. Harrison, A. M. Stephens, S. J. Devitt, and K. Nemoto, From quantum multiplexing to high-performance quantum networking, Nat. Photonics **4**, 792 (2010).

[38] O. A. Collins, S. D. Jenkins, A. Kuzmich, and T. A. B. Kennedy, Multiplexed Memory-Insensitive Quantum Repeaters, Phys. Rev. Lett. **98**, 060502 (2007).